Studies of the 2018/Mars Year 34 Planet-Encircling Dust Storm

S.D. Guzewich[1], A.A. Fedorova[2], M.A. Kahre[3], A.D. Toigo[4]

[1]NASA Goddard Space Flight Center, Greenbelt, MD, USA scott.d.guzewich@nasa.gov
[2]Space Research Institute (IKI), Moscow, Russia
[3]NASA Ames Research Center, Mountain View, CA, USA
[4]Johns Hopkins University Applied Physics Laboratory, Laurel, MD, USA

ABSTRACT

Mars' planet-encircling or global dust storms are an iconic and enigmatic feature of the Red Planet. Occurring every few Mars Years, on average, they are a stochastic process in the otherwise largely repeatable annual cycle of martian weather. In 2018 (Mars Year 34 in the calendar of Clancy et al. [2000]), an international fleet of spacecraft, 6 orbiters and 2 rovers, observed the most recent global dust storm. This introduction and the articles of this special collection describe the evolution and impacts of the storm from the surface to the exosphere, compare this storm to previous global dust storms, identify new phenomena never-before seen in such storms, and attempt to determine how and when global dust storms develop.

PLAIN LANGUAGE SUMMARY

Mars' planet-encircling or global dust storms are an iconic and enigmatic feature of the Red Planet. Occurring every few Mars Years, on average, they are a seemingly random process in the otherwise largely repeatable annual cycle of martian weather. In 2018, an international fleet of spacecraft, 6 orbiters and 2 rovers, observed the most recent global dust storm. This introduction and the articles of this special collection describe the evolution and impacts of the storm from the surface to the top of the atmosphere and beyond, compare this storm to previous global dust storms, identify new phenomena never-before seen in such storms, and attempt to determine how and when global dust storms develop.

KEY POINTS

- 6 orbiters and 2 rovers observed the 2018 Mars global dust storm
- The 27 papers of this special collection study the storm with observations, modeling, and theory
- The 2018 storm is the most comprehensively studied Mars global dust storm yet

1. INTRODUCTION

Spacecraft observations of martian "planet-encircling" or "global" dust storms extend back to Mariner 9, which famously arrived during the 1971 (Mars Year 9) global dust storm and

watched the storm decay from orbit [Leovy et al., 1971; Conrath et al., 1973; Pang and Hord, 1973]. Later, global dust storms were studied by the Viking orbiters and landers in 1977 (Mars Year 12) [Briggs et al., 1979; Ryan and Sharman, 1981], Mars Global Surveyor in 2001 (Mars Year 25) [Smith, 2004], and Mars Reconnaissance Orbiter [Wang and Richardson, 2015; Guzewich et al., 2017; Heavens et al., 2019a], Mars Odyssey [Smith, 2009], Mars Exploration Rovers [Lemmon et al., 2015], and Mars Express [Fedorova et al., 2018; Wolkenberg et al., 2018; Wolkenberg et al., 2020] in 2007 (Mars Year 28).

The global dust storm of 2018 (Mars Year 34) presented an unprecedented opportunity to study these rare and fascinating events that are unique in the Solar System. 8 spacecraft were on the surface or in orbit around the planet at the start of the storm, before the fatal reduction in sunlight ended the Opportunity rover's mission more than 14 years after its landing. Prior to its failure, Opportunity recorded the highest visible-band atmospheric dust opacity ever measured on the surface of Mars (>10). This special collection reflects studies of this global dust storm from 6 of the remaining 7 spacecraft and Earth-based telescopes that observed the growth, peak, and decay of the storm, and related modeling and theoretical studies to this particular dust storm and martian dust storms in general.

2. STORM EVOLUTION AND TIMELINE

The first confirmed global dust storm was observed by means of ground-based telescopes in Mars Year 1 - 1956 [Martin and Zurek, 1993]. The 2018/Mars Year 34 global dust storm was an equinoctial global dust storm, starting at approximately L_s = 185° [Sánchez-Lavega et al., 2019; Guzewich et al., 2019; Kass et al., 2019]. This was very nearly the same time of year that the 2001/Mars Year 25 global dust storm began, which represent the two earliest-starting global dust storms on record (Figure 1; Shirley et al., 2020).

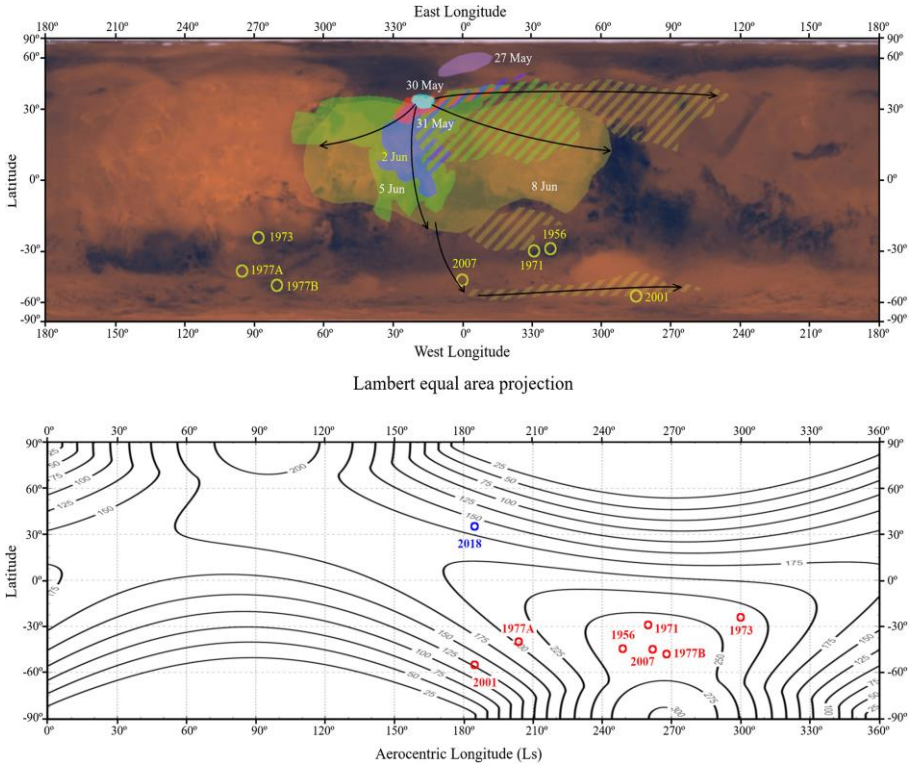

Figure 1: Figure 3 from Sánchez-Lavega et al. (2019). Maps of the 2018 Global Dust Storm (GDS) expansion and GDS occurrence. Upper: Lambert equal- area projection of Mars, showing the expanding area of the storm from 30 May to 8 June superimposed with different colors. The flat colors indicate the core of the storm, and the streaked regions indicate the total area. The purple area on 27 May corresponds to a precursor storm. The arrows indicate the directions followed by the expanding dust. Lower: Mean daily insolation (W/m2) at the top of the atmosphere along a Martian year (adapted from Sánchez- Lavega et al., 2018). The circles in both panels mark the onset location of the confirmed GDSs given in Table S1 from Sánchez-Lavega et al. (2019).

However, the MY34 storm was unique in its initiation in the northern hemisphere. All previous storms on record have been initiated in the southern hemisphere. This conforms with our (limited) knowledge about how global dust storms develop, which have been generally centered on the peak insolation (and accordingly the warmest and most vigorous atmospheric circulation) that Mars experiences each year (Figure 1b). Instead, the MY34 storm grew through a series of precursor storms in the northern hemisphere storm tracks that expanded south slowly toward the equator. Despite this unique feature, there are similarities with the growth trajectory of other global dust storms (such as 2007/Mars Year 28) which may have been initiated by "flushing" dust storms that cross the equator from the Acidalia/Chryse Planitia corridor [Wang et al., 2003]. But, the MY34 precursor storms were never truly "flushing" storms in that they never directly crossed the equator. Rather, (seemingly) independent southern polar cap edge dust lifting began and eventually merged with the northern hemisphere and equatorial storm region to

encircle the planet [Montabone et al., 2020]. This perhaps explains the comparatively methodical growth and expansion of the MY34 storm relative to previously observed global dust storms (particularly MY25 and MY28) which underwent explosive growth and expansion in the period of a few sols. This first growth phase of the storm was centered near Chryse Planitia and Meridiani Planum, which resulted in the eventual failure of the Opportunity rover.

This initial phase of the storm spread dust throughout the northern hemisphere and the growing southern polar cap edge dust lifting regions later sent dust over Gale Crater, where the Mars Science Laboratory Curiosity rover was exploring the Vera Rubin Ridge [Guzewich et al., 2019]. It also strengthened the atmospheric circulation and enhanced atmospheric thermal tides, which facilitated rapid spread of dust around the planet [Gillespie et al., 2020]. The strengthened Hadley circulation lofted dust to very high altitudes, ~70 km, and led to almost anvil-cloud like distributions of dust in the middle and upper atmosphere. Additionally, this seasonally atypically strong Hadley circulation produced dynamical heating of mid-altitude air at high latitudes in both hemispheres due to adiabatic warming in the descending branches of the equinoctial circulation [Shirley et al., 2019]. Indeed, both observations [Kass et al., 2019] and modeling [Bertrand et al., 2020] indicate that the northern hemisphere Hadley circulation remained strong, stronger even than the southern hemisphere Hadley circulation, past the peak of the storm (after L_s = 210°). Under typical seasonal evolution, the southern hemisphere circulation would have become dominant by that time.

Following this first burst of activity (~L_s = 185-192°), it seemed plausible that the dust in the atmosphere would begin to settle out of the atmosphere and the MY34 storm would have been better defined as a "large regional" dust storm. Heavens et al. [2019b] note that "The altitude of significant dust transport almost declined to prestorm levels…" near L_s = 194°. This brief pause or reduction in dust lifting can be seen in globally-averaged dust opacity (e.g., figures 7 and 10 by Montabone et al. [2020]) as a "knee" or change in slope of the opacity growth curve. But, a secondary "storm within a storm" [Montabone et al., 2020] over Tharsis that began at L_s = 197° injected massive amounts of dust into the atmosphere and made the storm truly "global" or "planet-encircling." This pause and then secondary expansion from the Tharsis dust lifting can be seen in Figure 2 from Smith [2019] using Mars Odyssey Thermal Emission Spectrometer retrievals of column dust optical depth.

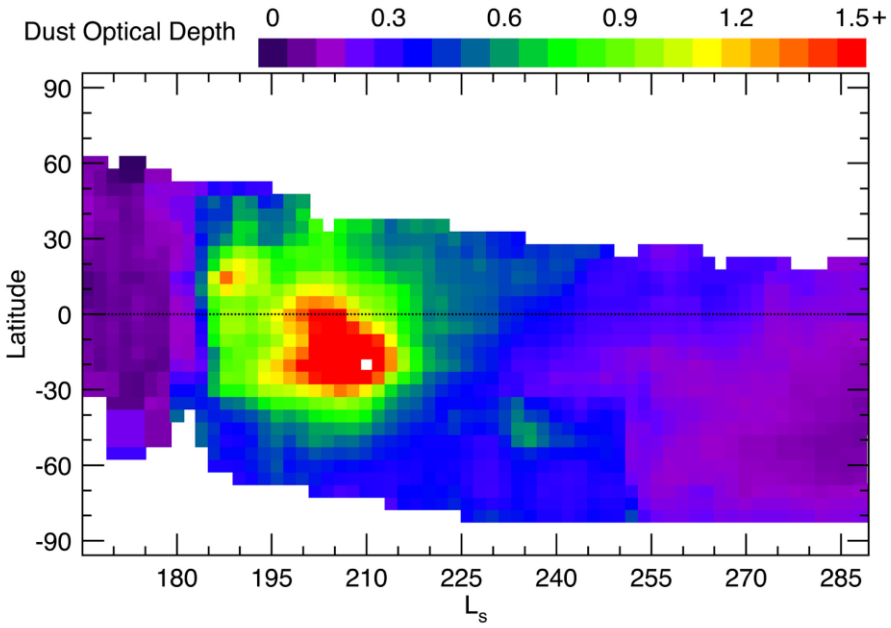

Figure 2. Figure 7a from Smith [2019]. THEMIS retrieved dust optical depth 1075 cm^{-1} scaled to an equivalent 6.1- mbar pressure surface to remove the effect of topography around the time of the MY 34 global dust storm. Shown is the zonal average as a function of time and latitude.

Bertrand et al. [2020] convincingly show that Hadley cell strengthening led to the Tharsis dust being lifted to very high altitudes (60-80 km) over a broad region. This high altitude dust injection was distinct in behavior from more mesoscale phenomena (e.g., "rocket dust storms"; Spiga et al. [2013]) that may produce detached dust layers in the middle atmosphere under normal dust conditions. Heavens et al. [2019b] and Bertrand et al. [2020] both note that this dust lifting was vigorously convective. This period of lifting after L_s = 197° also was distinct from "dusty deep convection" that was seen over Tharsis prior to this dust lifting region expanding and becoming the primary source of dust for the storm (see below; Heavens et al. [2019b]). The storm peaked, as measured by global atmospheric dust loading and middle atmospheric temperature, around L_s = 205-210° [Kass et al., 2019; Smith, 2019; Bertrand et al., 2020; Montabone et al., 2020]. After that point, it appears that dust sedimentation and deposition dominated behavior globally, which continued until dust returned to climatologically typical levels near L_s = 250°.

The long decay phase of the storm, from L_s = 210-250°, provides another point of comparison with previous global dust storms. Kass et al. [2019], Smith [2019], and Wolkenberg et al. [2020] all note that the MY34 storm decayed faster than either the MY25 or MY28 storms. However, the Curiosity rover observed a decay timescale of column dust opacity identical to that observed by the Spirit and Opportunity rovers during the MY28 storm [Guzewich et al., 2019]. Reconciling those disparate observations likely falls to regional vs. global perspectives, as Curiosity was never near the core of major dust lifting centers. The decay rate of global storms

is plausibly driven by a combination of atmospheric circulation structure and strength, height of dust during the storm, and dust particle size distribution, all of which help determine the timescale for a dust particle to sediment out of the atmosphere to the surface. For MY34, we know that dust was lifted to great altitudes (e.g., Heavens et al. [2019]) and we know that dust particle sizes were very large (at least over Gale Crater; Lemmon et al. [2019]). Bertrand et al. [2020] noted that the storm's decay timescale was particularly sensitive to dust particle size in their simulations. One factor that appears distinct for MY34 relative to the MY25 and MY28 storms (for which we have the most comprehensive data and modeling for comparison; e.g., see Smith [2004] for the MY25 thermal structure) is the atmospheric circulation structure, with a strong northern hemisphere Hadley cell well into southern hemisphere spring. Future work should investigate whether the seasonally-driven collapse of this structure, coupled with the decay of the global dust storm, could have resulted in a faster storm decay relative to the MY25 and MY28 storms which were centered in the seasonally-favored southern hemisphere Hadley circulation. Similarly, globally heterogeneous dust populations, with different particle size distributions lifted during different global dust storms, should be explored.

Mars Year 34 also provided an important control experiment for understanding how some storms become global, while others remain regional. Soon after the InSight lander arrived at Elysium Planitia, a strong regional dust storm developed at L_s = 320° [Banfield and Spiga et al., 2020]. This storm began in western Chryse Planitia, near where the global dust storm had begun just months before [Montabone et al., 2020]. This is an important note, as surface dust source exhaustion from dust storms and the "recharge" timescale from airfalling dust, is an ongoing topic of study and speculation (Bertrand et al. [2020] also discusses this for the global dust storm). This regional storm spread dust around the planet in both hemispheres, but the storm ceased dust lifting and decayed on a timescale of days to weeks rather than months. Some observations of these storms have helped distinguish global from regional storms and perhaps provide criteria to anticipate global expansion of a storm in the future. Kass et al. [2019] note that daytime 50 Pa temperatures exceed 235 K in global storms, more than 10 K higher than regional storms, and a temperature > 220 K in the tropics is even more discriminatory (observed regional storms have never exceeded 205 K). Additionally, the rapid expansion of 50 Pa warmth (> 200 K from 45°S-45°N within 2° of solar longitude) is also unique to global storms in the Mars Climate Sounder (MCS) record.

3. PERSPECTIVE FROM THE SURFACE

Curiosity's measurements in Gale Crater during the storm with the Rover Environmental Monitoring System (REMS) were the first such meteorological measurements from the surface since the Viking landers and the first ever near the equator during a global dust storm [Guzewich et al., 2019; Viúdez-Moreiras et al., 2019]. The initial phase of storm growth near Opportunity's location in Meridiani Planum did not substantively impact local conditions in Gale Crater. Dust lifted in the southern hemisphere eventually reached Gale after L_s = 192°, which eventually resulted in a peak dust optical depth of ~8.5 [Guzewich et al., 2019]. This dust optical depth

reduced UV light at the surface by ~90%, lowering the daytime air and ground temperatures. Nighttime temperatures warmed due to increased downwelling infrared radiation from the dust (Figure 3, Viúdez-Moreiras et al. [2019]). This reduction in the diurnal surface temperature range was also seen globally from orbit. Streeter et al. [2019] note that nighttime warming from longwave dust emission more than compensated for daytime reductions in shortwave insolation, resulting in a general increase in diurnally averaged temperatures. This, however, is modulated by the thermal inertia of an individual location. Comparing with the MY28 storm, Wolkenberg et al. [2020] note that surface temperatures converge to near 250 K once 9 μm dust opacity exceeds 1-2 and Streeter et al. [2019] also note asymptotic behavior of daytime surface temperatures at increasing dust opacity.

Atmospheric pressure tides responded dramatically, with the semidiurnal tide (long known to be responsive to globally-integrated dust loading [Wilson and Hamilton, 1996]) briefly becoming stronger than the diurnal tide in Gale Crater. The global response of the martian water cycle to such storms is becoming clearer (see below), but never before had humidity been measured *in situ* during a global dust storm. In Gale Crater, the humidity decreased due to the warmer nighttime temperatures, but the amount of water vapor itself increased sharply (by almost a factor of 2) with the arrival of significant dust opacity before decreasing again to pre-storm levels after ~40 sols (Figure 3, Viúdez-Moreiras et al. [2019]). The mechanism behind these fluctuations is unknown, but needs to be understood in the context of higher water vapor mixing ratios seen by Curiosity in MY34 relative to previous years.

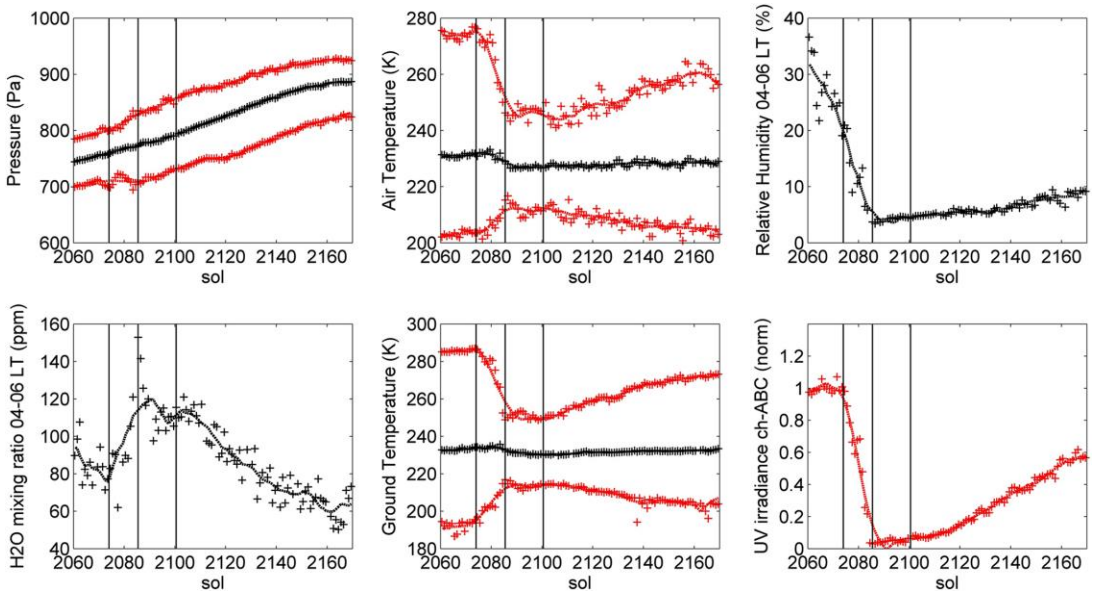

Figure 3. Figure 3 from Viúdez-Moreiras et al. [2019]. Evolution of REMS variables (sols 2060–2170) for the period encompassing the onset (sols 2075–2084), highly dusty (sols 2085–2100), and decay phases of the GDS. Daily mean, maximum, and minimum values are shown for pressure (top left) and temperatures (top and bottom middle), while the relative humidity (top right) and water mixing ratio (bottom left) values correspond to values where the relative humidity reaches its maximum (between

4:00 and 6:00 LTST) and their uncertainty is lower. Finally, the daily maximum ultraviolet (UV) irradiance (f) is shown normalized to the value on sol 2070. A 20- sol mobile average is also shown for each variable for a better visualization. As in Figure 2, vertical lines show the start times of the GDS onset (sol 2075), highly dusty (sol 2085), and decay (sol 2100) phases in Gale Crater.

The double-peaked structure seen in water vapor mixing ratio, air temperature, and even pressure is reflective of two pulses of dust that entered Gale Crater. Smith et al. [2019] show that in-crater dust extinction (extinction as measured along a line-of-sight from the Curiosity rover to the Gale Crater rim) was an order of magnitude higher than anything measured prior to the global dust storm. Horizontal visibility dropped to <3 km, whereas it normally equals or exceeds 30 km and sometimes 70 km or more. The peak in in-crater dust extinction was also 3-5 sols after the column dust opacity peak. And while the atmospheric column dust opacity showed a generally steady decline of dust opacity after the initial peak [Guzewich et al., 2019], the in-crater dust extinction had a second peak approximately 25 sols after the initial wave of dust. In conjunction with the REMS variables, this points to dynamical behavior of dust moving above the crater and then dust sedimenting to lower altitudes within the crater over time. This behavior is further supported by analysis of dust particle sizes, which corroborate the two-peaked pattern of in-crater dust extinction [Lemmon et al., 2019]. In combination, Lemmon et al. [2019], Smith et al. [2019], Viúdez-Moreiras et al. [2019], and Guzewich et al. [2019] show that the first wave of dust predominantly passed *above* Gale Crater with dust particle effective radii as high as 8 μm, the largest ever observed in Mars' atmosphere. These large dust particles sedimented quickly to lower altitudes within the crater, producing a delayed peak in in-crater dust extinction. Then a second wave of dust arrived at Gale Crater approximately 25 sols later, but this wave arrived at lower altitudes directly in the crater and did not make a clear change to the *column* dust opacity. Given Mars' thin atmosphere, dust particles with such large effective radii should sediment to the surface on very short timescales (hours or sols) without compensating upward vertical motion in the atmosphere. The lack of any clear signs of local dust lifting within Gale Crater by wind stress or dust devil lifting [Guzewich et al., 2019] imply that these very large particles were transported aloft over hundreds to thousands of kilometers distance, emphasizing the vigorous and highly anomalous dynamics that were likely ongoing within the storm.

4. UPPER ATMOSPHERE RESPONSE

Recent work prior to the MY34 global dust storm showed that dust storms likely have a disproportionate effect on Mars' loss of water to space in the modern climate epoch [Chaffin et al., 2014; 2017; Heavens et al., 2018; Fedorova et al., 2018]. The presence of the Mars Reconnaissance Orbiter (MRO), Mars Atmosphere and Volatile Evolution mission (MAVEN), and the ExoMars/Trace Gas Orbiter (TGO) simultaneously during a global dust storm provided an opportunity to watch this behavior through the entire atmospheric column and diagnose the

mechanisms that lift water to high altitude where it can be photodissociated to be a direct source of hydrogen atoms in the thermosphere.

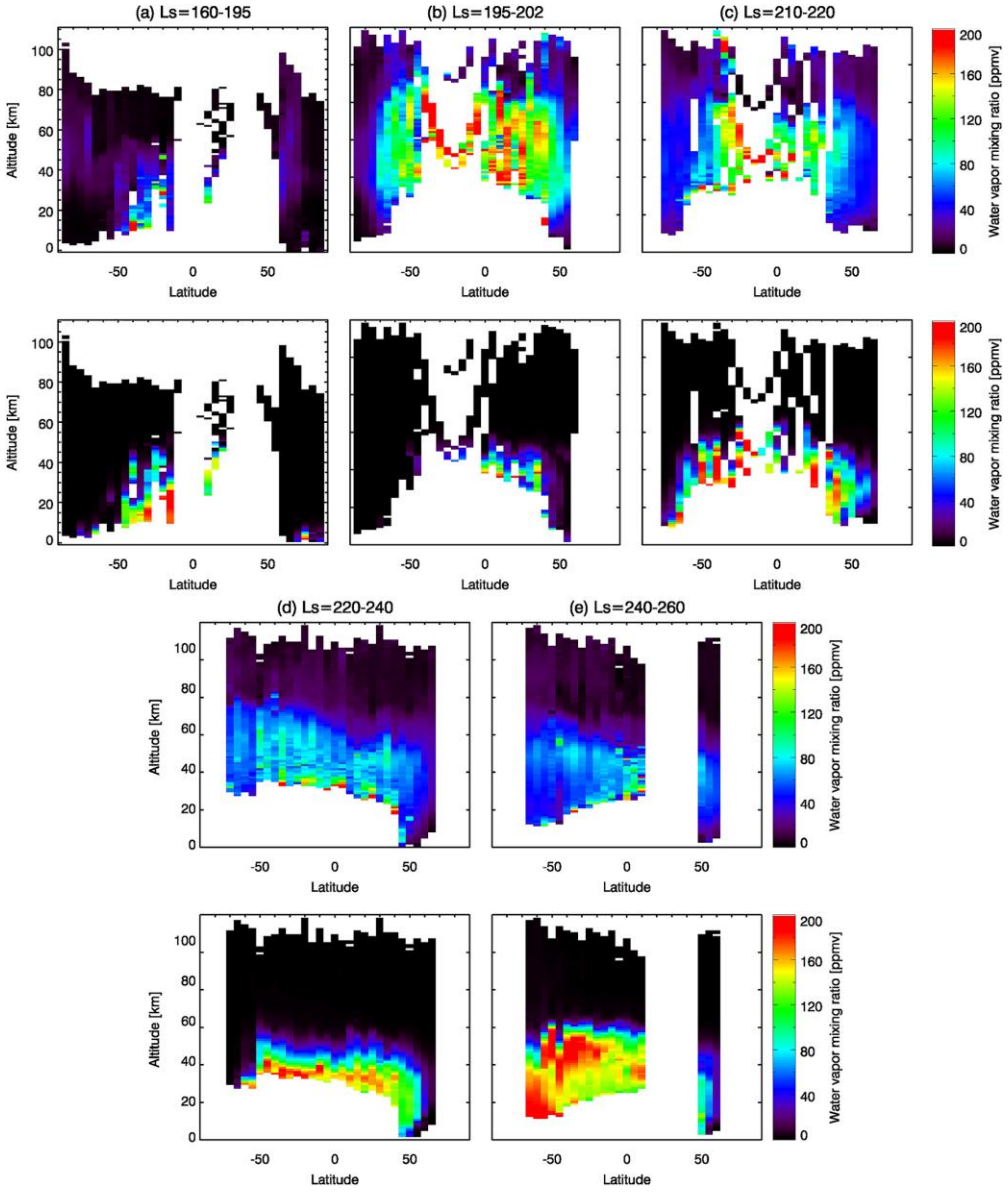

Figure 4. Figure 6 from Aoki et al. [2019]. Latitudinal variation of the water vapor vertical profiles retrieved from NOMAD data (the top panels of (a)–(e)), predicted by the GEM- Mars for non- dust storm conditions (the bottom panels of (a)–(e)) in the seasonal range between *Ls* = 160°–195° (Figure 6a, before the global dust storm), *Ls* = 195°–202° (Figure 6b, during the growth phase of the storm), *Ls* = 210°–220° (Figure 6c, during the mature phase of the storm), *Ls* = 220°–240° (Figure 6d, during the decay phase of the storm), and *Ls* = 240°–260° (Figure 6e, during the decay phase of the storm). The retrievals and GEM predictions are binned in 5° latitude × 1 km altitude grid (averaged in season and longitude).

Aoki et al. [2019] show that great amounts of water were lifted to altitudes as high as 100 km during the storm. Using solar occultation, the Nadir and Occultation for Mars Discovery (NOMAD) instrument onboard TGO can measure water vapor abundance with high precision and vertical resolution. As seen in Figure 4, this change occurred rapidly after the storm began and persisted through its duration. Interestingly, similar, if less intense, behavior occurred during the late winter large regional dust storm in MY34. The Atmospheric Chemistry Suite (ACS) also onboard TGO similarly saw water ice clouds at exceptionally high altitudes, greater than 90 km during the storm, with water ice particle effective radii (~1.5 μm) typical of much lower altitudes [Stcherbinine et al., 2020]. As in the case of Curiosity (see Section 3), these large particle effective radii at high altitudes imply that strong upward motion was likely occurring within the storm.

Neary et al. [2019] used a Mars general circulation model (GCM) to diagnose the mechanisms behind the dramatic increase in high-altitude water vapor described by Aoki et al. [2019]. They found that although the atmospheric circulation is deepened and strengthened during the storm, it alone is not sufficient to transport water vapor to such high altitudes. More directly, they find that the altitude of the hygropause (typically in Mars' atmosphere where water ice clouds occur and water vapor is scarce above) is driven by the vertical profile of dust. Increased high-altitude dust during the storm warms the middle atmosphere and thus shifts the hygropause to much higher altitudes, letting water vapor reach altitudes where it is photodissociated.

The effects of the storm reached into the ionosphere and thermosphere. Heating of the lower atmosphere by the dust storm causes the entire atmosphere to expand, which raises ionospheric altitudes. This phenomena was noted back to Mariner 9 [Hantsch & Bauer, 1990].

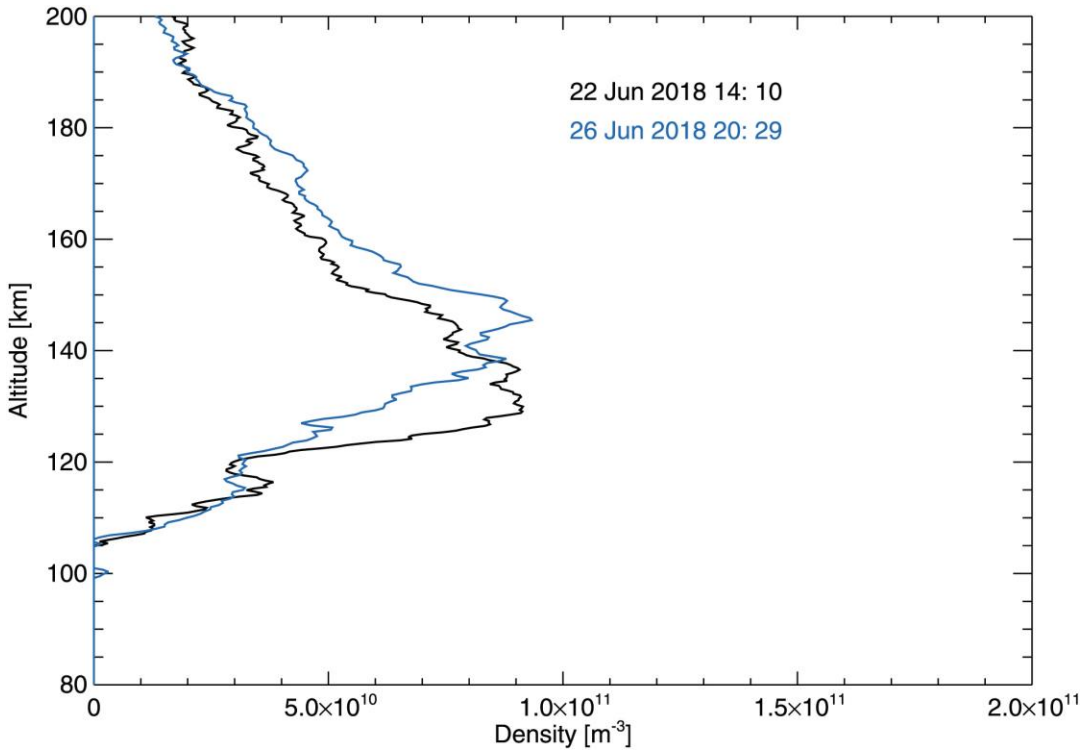

Figure 5. Figure 4 from Felici et al. [2020]. MAVEN Radio Occultation Science Experiment egress electron density profiles from 22 June 2018 and 26 June 2018. Electron density uncertainties are 1.85×109 m−3 for each profile.

This increase in ionospheric peak altitude was again noted during the MY34 global dust storm by a variety of spacecraft and techniques. Felici et al. [2020] noted a 10-15 km increase in peak ionospheric altitude using MAVEN radio occultation retrievals (Figure 5). Girazian et al. [2019] saw similar behavior with the Mars Express Mars Advanced Radar for Subsurface and Ionosphere Sounding and contextualized that change with the long observation history of Mars Express through multiple large regional dust storms and two global dust storms. The ionospheric peak altitude was also highly variable following the initial global expansion in late June 2018. This change in ionospheric altitude alters to chemical composition of the upper atmosphere during the storm. While the upward shift in the ionosphere increases the production of hot oxygen ("hot O"), the expansion of the neutral atmosphere increases the collisional loss of hot O. In combination, this reduced the oxygen escape rate during the storm by approximately 28% [Lee et al., 2020].

Heating and expansion of the neutral martian atmosphere was also observed. This was manifested in a near-doubling of CO_2 density on the planet's nightside at thermospheric altitudes (110 km) seen by MAVEN [Chaufray et al., 2019]. MAVEN observed a near 20 K temperature increase in the thermosphere, while also seeing cooling at equatorial latitudes near the start of the storm due to adiabatic cooling in strong upward motion [Jain et al., 2020]. These density and

temperature changes were used to diagnose the atmospheric circulation, and indicate that a two-cell meridional circulation was still present during the storm (as was also seen in the lower atmosphere, Section 2) which created dynamical effects in the northern hemisphere [Jain et al., 2020; Girazian et al., 2019].

5. NEW PHENOMENA

The diversity of observations of the storm—diversity of location, instrument, and local time coverage—allowed a number of new phenomena to be discovered. Since the MY28 global dust storm, the Mars Climate Sounder began a "cross-track" observation to expand the number of local times it observes. These observations helped identify a dramatic diurnal variation in dust during the global storm, particularly at high southern latitudes. Kleinböhl et al. [2019] demonstrate 20-40 km changes of the effective dust "top" between morning and afternoon and link this behavior to an enhanced diurnal tide during the storm. Indeed they show that the remnant southern winter polar vortex rotated fully around the pole each day as the diurnal tide propagated westward and replicated this behavior in a Mars GCM. This remnant polar vortex, with high potential vorticity, was somewhat impervious to mixing with the exterior low potential vorticity and dusty atmosphere. Hernández-Bernal et al. [2019] used Mars Express camera images to show graceful dust streamers crossing the day-night terminator over the south pole, illuminated later than the surface due to their high altitude (Figure 6). Their shape and movement, which could be tracked over multiple images to estimate wind speed, serve as tracers of polar atmospheric dynamics during the storm. Hence, these arcs of dust may be structured by filaments of potential vorticity within the polar vortex.

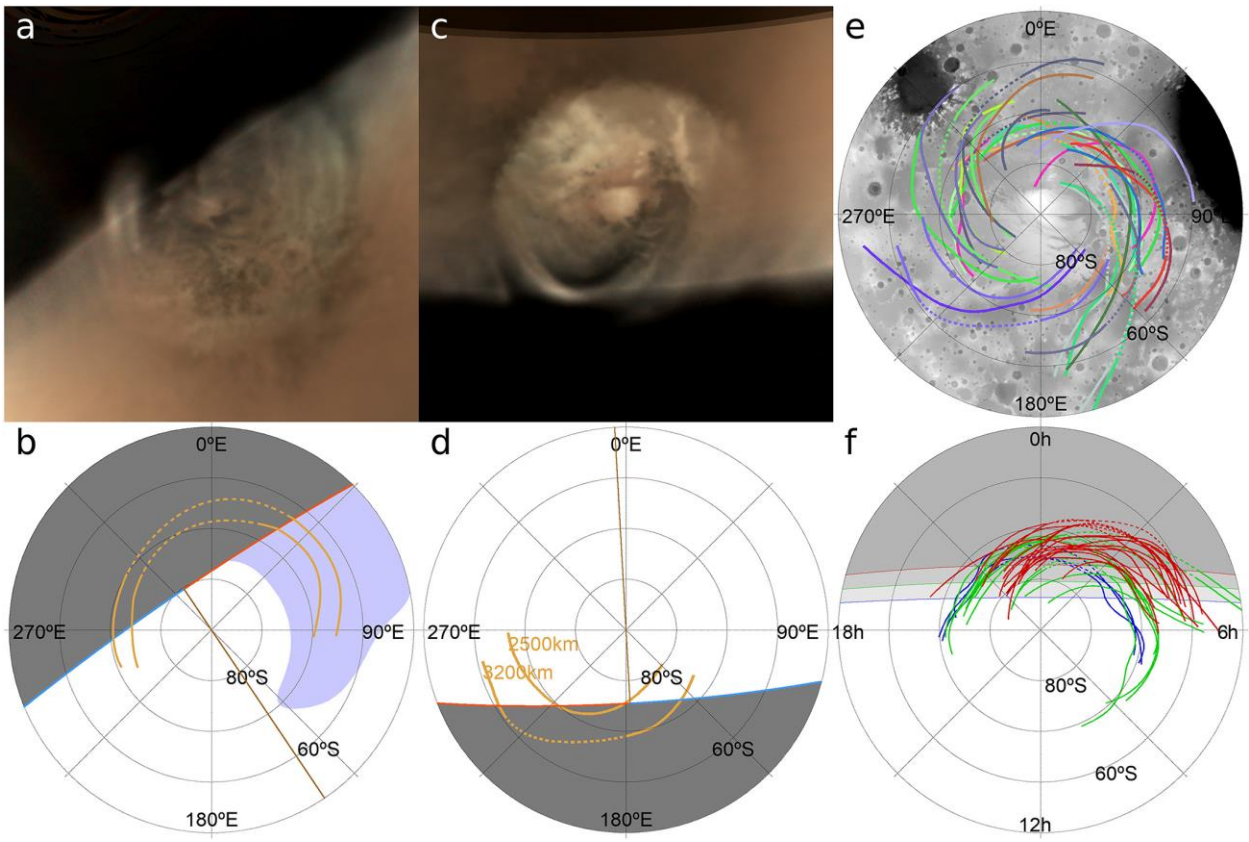

Figure 6. Figure 2 from Hernández-Bernal et al. [2019]. Images and structure of the arc bands around the south pole. (a, c) Polar projected images of the Southern Polar Region on 1 July, 17:30 UT and 22 July, 16:40 UT, respectively. (b, d) Schematic representations of previous images showing the nightside (dark gray), the morning hazes (blue lilac), and the observed bands, with continuous orange lines indicating visible parts and dotted sections indicating the potential location in the nightside, Numbers in orange indicate the estimated length of arcs. Red and blue lines indicate morning and evening terminators, and the brown line indicates the subsolar meridian. Notice the absence of morning hazes and the presence of a fully visible band on 22 July. (e) Areographic distribution of measured bands over a gray topographic map made from MOLA data (Smith et al., 1999) (different colors represent different observations). (f) Graph showing the latitude- local time distribution of all the observed bands. Different band colors indicate different periods starting on 18 June (blue), 1 July (green), and 18 July (red). Gray areas represent the night.

MAVEN also observed a new phenomena near the day-night terminator. Connour et al. [2020] discovered a persistent water ice cloud band along and just beyond the evening terminator that sometimes spanned 6000 km in latitude (Figure 7). GCM modeling indicated that altered atmospheric tides during the storm produced colder conditions near the dawn and dusk terminators, facilitating the formation of expansive water ice clouds. MAVEN's orbit precluded confirmation of corresponding morning terminator clouds.

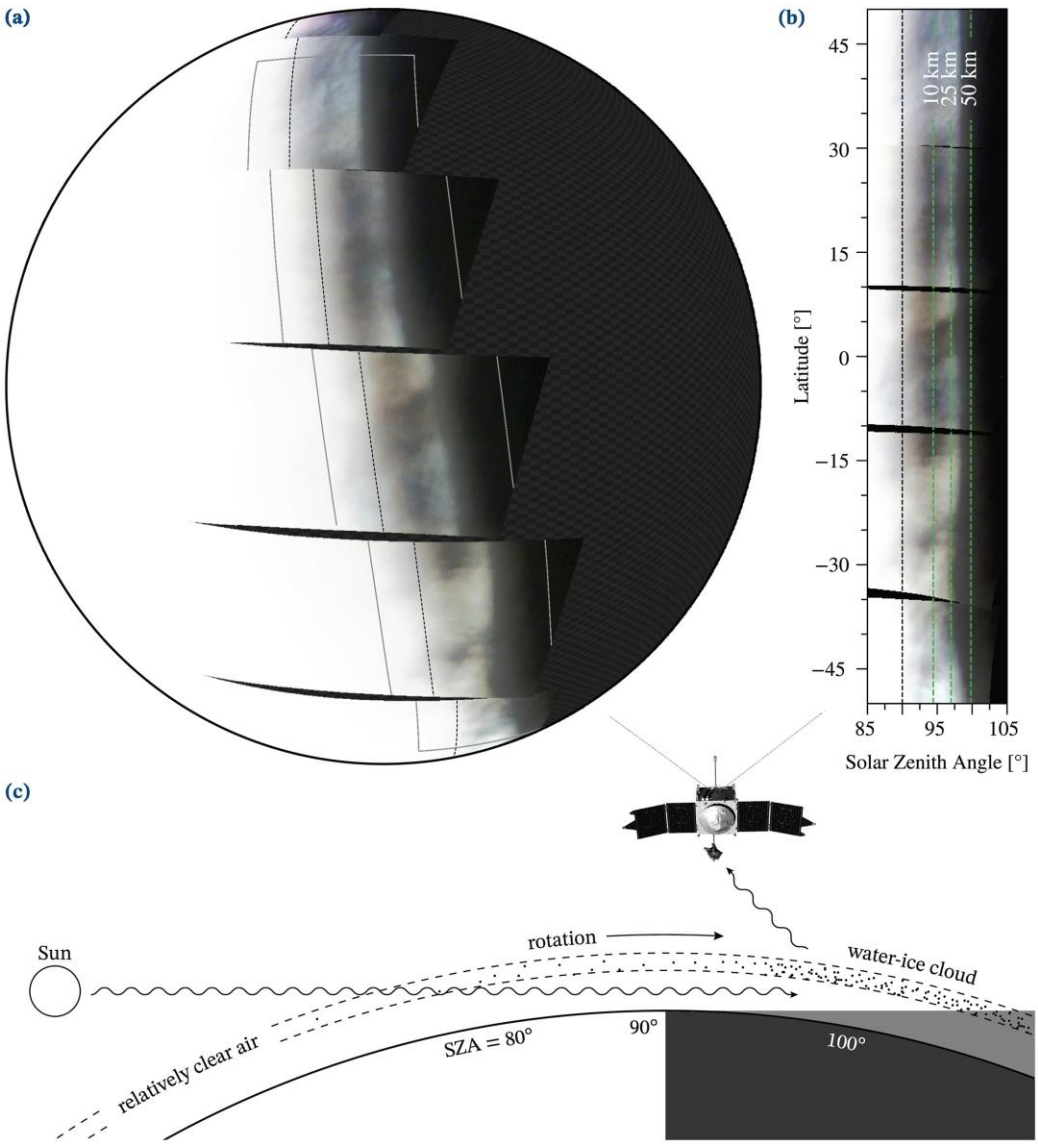

Figure 7. Figure 1 from Connour et al. [2020]. Composite graphic describing the observations, illuminated altitudes, and physical interpretation of a twilight cloud band. (a) Example projection of a latitudinally continuous twilight cloud band taken shortly after the start of the mature phase of the GDS (orbit 7281; L_s 200°). This false- color projection represents what each swath would have looked like when viewed from the position of the spacecraft at apoapsis. The black dashed line denotes the location of the terminator, and the gray box denotes the bounds of Figure 1b. (b) Minimum illuminated altitudes of the cloud band. Solar zenith angles were converted into minimum altitudes at which these aerosols must be directly illuminated, which reveals that bands often reached altitudes of at least 40 to 50 km. (c) A schematic, cross- sectional representation of IUVS viewing geometry. Incoming ultraviolet solar radiation did not interact with water vapor and encountered few, if any, water- ice clouds before

illuminating this band from below. Some light was scattered through these clouds directly to the spacecraft. Schematic not to scale.

In the upper atmosphere, MAVEN was able to also measure how the bulk composition of the atmosphere changed in response to the storm. As stated above, the thermosphere warmed and expanded during the storm, leading to higher atmospheric densities [Chaufray et al., 2019]. In conjunction, CO_2 and Ar densities increased in the thermosphere, but surprisingly, atomic O density *decreased* by 20% [Elrod et al., 2019]. Thus far, there is no explanation for this change but this implies that unknown dynamical and/or photochemical activities were occurring within the thermosphere as the storm expanded near the surface.

Atmospheric modeling helped expand and contextualize many of the results presented in this special collection. The increasing sophistication of Mars atmospheric modeling, like the expansion of spacecraft observations, has also led to new insights. Of particular note, Bertrand et al. [2020] used tracer tagging to watch how dust particles are lifted, transported, sedimented, and relifted during their simulation of the MY34 global dust storm. They show that transfer of dust between the Tharsis region and Arabia Terra/Terra Sabeae may have helped precondition the Tharsis region for the "storm within the storm" that Montabone et al. [2020] find expanded the storm to global proportions. Understanding the dynamics of how dust is moved through different surface reservoirs may be of critical importance to understanding why some storms become global while most do not.

6. CONCLUSIONS

The 2018/Mars Year 34 planet-encircling dust storm provided a unique opportunity to study these iconically martian events. The introduction and the works included in this special collection serve as a foundation for future analysis of this storm, comparison with previous and future storms, and critical data points to understand how global dust storms develop and shape the modern climate. The upcoming arrival of new spacecraft, the continued advance of modeling and theoretical understanding, and eventual human exploration will surely provide additional insights to understanding Mars' modern climate and its unique planet-wide dust storms.

REFERENCES

Aoki, S., Vandaele, A. C., Daerden, F., Villanueva, G. L., Liuzzi, G., Thomas, I. R., et al. (2019). Water vapor vertical profiles on Mars in dust storms observed by TGO/NOMAD. *Journal of Geophysical Research: Planets*, 124, 3482– 3497. https://doi.org/10.1029/2019JE006109

Bertrand, T., Wilson, R. J., Kahre, M. A., Urata, R., & Kling, A. (2020). Simulation of the 2018 global dust storm on Mars using the NASA Ames Mars GCM: A multitracer approach. *Journal of Geophysical Research: Planets*, 125, e2019JE006122. https://doi.org/10.1029/2019JE006122

Briggs, G. A., Baum, W. A., and Barnes, J. (1979), Viking Orbiter imaging observations of dust in the Martian atmosphere, *J. Geophys. Res.*, 84(B6), 2795– 2820, doi:10.1029/JB084iB06p02795.

Chaffin, M. S., Deighan, J., Schneider, N. M., & Stewart, A. I. F. (2017). Elevated atmospheric escape of atomic hydrogen from Mars induced by high- altitude water. *Nature Geoscience*, 10, 174– 178. https://doi.org/10.1038/ngeo2887

Chaufray, J.- Y., Chaffin, M., Deighan, J., Jain, S., Schneider, N., Mayyasi, M., & Jakosky, B. (2020). Effect of the 2018 Martian global dust storm on the CO_2 density in the lower nightside thermosphere observed from MAVEN/IUVS Lyman- alpha absorption. *Geophysical Research Letters*, 47, e2019GL082889. https://doi.org/10.1029/2019GL082889

Connour, K., Schneider, N. M., Milby, Z., Forget, F., Alhosani, M., Spiga, A., et al. (2020). Mars's twilight cloud band: A new cloud feature seen during the Mars Year 34 global dust storm. *Geophysical Research Letters*, 47, e2019GL084997. https://doi.org/10.1029/2019GL084997

Conrath, B., Curran, R., Hanel, R., Kunde, V., Maguire, W., Pearl, J., Pirraglia, J., Welker, J., and Burke, T.(1973), Atmospheric and surface properties of Mars obtained by infrared spectroscopy on Mariner 9, *J. Geophys. Res.*, 78(20), 4267– 4278, doi:10.1029/JB078i020p04267.

Clancy, R. T., Sandor, B. J., Wolff, M. J., Christensen, P. R., Smith, M. D., Pearl, J. C., Conrath, B. J., & Wilson, R. J. (2000). An intercomparison of ground- based millimeter, MGS TES, and Viking atmospheric temperature measurements: Seasonal and interannual variability of temperatures and dust loading in the global Mars atmosphere. *Journal of Geophysical Research*, 105(E4), 9553– 9571. https://doi.org/10.1029/1999JE001089

Elrod, M. K., Bougher, S. W., Roeten, K., Sharrar, R., & Murphy, J. (2020). Structural and Compositional Changes in the Upper Atmosphere Related to the PEDE- 2018 Dust Event on Mars as Observed by MAVEN NGIMS. *Geophysical Research Letters*, 47, e2019GL084378. https://doi.org/10.1029/2019GL084378

Fedorova, A., Bertaux, J.- L., Betsis, D., Montmessin, F., Korablev, O., Maltagliati, L., & Clarke, J.(2018). Water vapor in the middle atmosphere of Mars during the 2007 global dust storm. *Icarus*, 300, 440– 457. https://doi.org/10.1016/j.icarus.2017.09.025

Felici, M., Withers, P., Smith, M. D., González- Galindo, F., Oudrhiri, K., & Kahan, D. (2020). MAVEN ROSE observations of the response of the Martian ionosphere to dust storms.

Journal of Geophysical Research: Space Physics, 125, e2019JA027083. https://doi.org/10.1029/2019JA027083

Gillespie, H. E., Greybush, S. J., & Wilson, R. J. (2020). An investigation of the encirclement of Mars by dust in the 2018 global dust storm using EMARS. *Journal of Geophysical Research: Planets*, 125, e2019JE006106. https://doi.org/10.1029/2019JE006106

Girazian, Z., Luppen, Z., Morgan, D. D., Chu, F., Montabone, L., Thiemann, E. M. B., et al. (2020). Variations in the ionospheric peak altitude at Mars in response to dust storms: 13 years of observations from the Mars Express Radar Sounder. *Journal of Geophysical Research: Planets*, e2019JE006092 125, https://doi.org/10.1029/2019JE006092

Guzewich, S.D., A.D. Toigo, H. Wang (2017), An Investigation of Dust Storms Observed with the Mars Color Imager, Icarus, 289, 199-213, http://dx.doi.org/10.1016/j.icarus.2017.02.020.

Guzewich, S. D., Lemmon, M., Smith, C. L., Martínez, G., de Vicente- Retortillo, Á., Newman, C. E., et al. (2019). Mars Science Laboratory observations of the 2018/Mars year 34 global dust storm. *Geophysical Research Letters*, 46, 71– 79. https://doi.org/10.1029/2018GL080839

Heavens, N. G., Kleinböhl, A., Chaffin, M. S., Halekas, J. S., Kass, D. M., Hayne, P. O., McCleese, D. J., Piqueux, S., Shirley, J. H., & Schofield, J. T. (2018). Hydrogen escape from Mars enhanced by deep convection in dust storms. *Nature Astronomy*, 2, 126– 132.

Heavens, N. G., D. M. Kass, J. H. Shirley, S. Piqueux, and B. A. Cantor (2019a). An Observational Overview of Dusty Deep Convection in Martian Dust Storms. *J. Atmos. Sci.*, **76**, 3299–3326, https://doi.org/10.1175/JAS-D-19-0042.1.

Heavens, N. G., Kass, D. M., & Shirley, J. H. (2019b). Dusty deep convection in the Mars Year 34 planet- encircling dust event. *Journal of Geophysical Research: Planets*, 124, 2863– 2892. https://doi.org/10.1029/2019JE006110

Hernández- Bernal, J., Sánchez- Lavega, A., del Río- Gaztelurrutia, T., Hueso, R., Cardesín- Moinelo, A., Ravanis, E. M., et al. (2019). The 2018 Martian global dust storm over the South Polar Region studied with MEx/VMC. *Geophysical Research Letters*, 46, 10330– 10337. https://doi.org/10.1029/2019GL084266

Jain, S. K., Bougher, S. W., Deighan, J., Schneider, N. M., Gonzalez- Galindo, F., Stewart, A. I. F., et al. (2020). Martian thermospheric warming associated with the Planet Encircling Dust Event of 2018. *Geophysical Research Letters*, 47, e2019GL085302. https://doi.org/10.1029/2019GL085302

Kass, D. M., Schofield, J. T., Kleinböhl, A., McCleese, D. J., Heavens, N. G., Shirley, J. H., & Steele, L. J.(2019). Mars Climate Sounder observation of Mars' 2018 global dust storm. *Geophysical Research Letters*, 46. https://doi.org/10.1029/2019GL083931

Kleinböhl, A., Spiga, A., Kass, D. M., Shirley, J. H., Millour, E., Montabone, L., & Forget, F. (2020). Diurnal variations of dust during the 2018 global dust storm observed by the Mars Climate Sounder. *Journal of Geophysical Research: Planets*, 125, e2019JE006115. https://doi.org/10.1029/2019JE006115

Lee, Y., Fang, X., Gacesa, M., Ma, Y., Tenishev, V., Mahaffy, P., et al. (2020). Effects of global and regional dust storms on the Martian hot O corona and photochemical loss. *Journal of Geophysical Research: Space Physics*, 125, e2019JA027115. https://doi.org/10.1029/2019JA027115

Lemmon, M. T., Wolff, M. J., Bell, J. F. III, Smith, M. D., Cantor, B., & Smith, P. H. (2015). Dust aerosol, clouds, and the atmospheric optical depth record over 5 Mars years of the Mars Exploration Rover mission. *Icarus*, 251, 96–111. https://doi.org/10.1016/j.icarus.2014.03.029.

Lemmon, M. T., Guzewich, S. D., McConnochie, T., de Vicente- Retortillo, A., Martínez, G., Smith, M. D., et al. (2019). Large dust aerosol sizes seen during the 2018 Martian global dust event by the Curiosity rover. *Geophysical Research Letters*, 46, 9448– 9456. https://doi.org/10.1029/2019GL084407

Leovy, C.B., G.A. Briggs, A.T. Young, B.A. Smith, J.B. Pollack, E.N. Shipley, and R.L. Wildey (1971). The martian atmosphere: Mariner 9 television experiment progress report. Icarus, 17(2), 373-393. https://doi.org/10.1016/0019-1035(72)90006-1.

Martin, L. J., and Zurek, R. W. (1993), An analysis of the history of dust activity on Mars, *J. Geophys. Res.*, 98(E2), 3221– 3246, doi:10.1029/92JE02937.

Montabone, L., Spiga, A., Kass, D. M., Kleinboehl, A., Forget, F., & Millour, E. (2020). Martian year 34 column dust climatology from mars climate sounder observations: Reconstructed maps and model simulations. *Journal of Geophysical Research: Planets*, 125, e2019JE006111. https://doi.org/10.1029/2019JE006111

Neary, L., Daerden, F., Aoki, S., Whiteway, J., Clancy, R. T., Smith, M., et al. (2020). Explanation for the increase in high- altitude water on Mars observed by NOMAD during the 2018 global dust storm. *Geophysical Research Letters*, 47, e2019GL084354. https://doi.org/10.1029/2019GL084354

Pang, K. and C.W. Hord (1973), Mariner 9 ultraviolet spectrometer experiment: 1971 Mars dust storm. Icarus, 18(3), 481-488. https://doi.org/10.1016/0019-1035(73)90157-7.

Ryan, J. A., and Sharman, R. D. (1981), Two major dust storms, one Mars year apart: Comparison from Viking data, *J. Geophys. Res.*, 86(C4), 3247– 3254, doi:10.1029/JC086iC04p03247.

Sánchez- Lavega, A., del Río- Gaztelurrutia, T., Hernández- Bernal, J., & Delcroix, M. (2019). The onset and growth of the 2018 Martian Global Dust Storm. *Geophysical Research Letters*, 46, 6101– 6108. https://doi.org/10.1029/2019GL083207

Shirley, J. H., Kleinböhl, A., Kass, D. M., Steele, L. J., Heavens, N. G., Suzuki, S., et al. (2020). Rapid expansion and evolution of a regional dust storm in the Acidalia Corridor during the initial growth phase of the Martian global dust storm of 2018. *Geophysical Research Letters*, 47, e2019GL084317. https://doi.org/10.1029/2019GL084317

Shirley, J. H., McKim, R. J., Battalio, J. M., & Kass, D. M. (2020). Orbit- spin coupling and the triggering of the Martian planet- encircling dust storm of 2018. *Journal of Geophysical Research: Planets*, 125, e2019JE006077. https://doi.org/10.1029/2019JE006077

Smith, C. L., Moores, J. E., Lemmon, M., Guzewich, S. D., Moore, C. A., Ellison, D., & Khayat, A. S. J. (2019). Visibility and line- of- sight extinction estimates in Gale Crater during the 2018/MY34 global dust storm. *Geophysical Research Letters*, 46, 9414– 9421. https://doi.org/10.1029/2019GL083788

Smith, M.D. (2004). Interannual variability in TES atmospheric observations of Mars during 1999-2003. Icarus, 167(1), 148-165. https://doi.org/10.1016/j.icarus.2003.09.010.

Smith, M.D. (2009). THEMIS observations of Mars aerosol optical depth from 2002-2008. Icarus, 202(2), 444-452. https://doi.org/10.1016/j.icarus.2009.03.027

Smith, M. D. (2019). THEMIS Observations of the 2018 Mars Global Dust Storm. *Journal of Geophysical Research: Planets*, 124, 2929– 2944. https://doi.org/10.1029/2019JE006107

Spiga, A., Faure, J., Madeleine, J. B., Määttänen, A., & Forget, F. (2013). Rocket dust storms and detached dust layers in the Martian atmosphere. *Journal of Geophysical Research: Planets*, 118, 746– 767. https://doi.org/10.1002/jgre.20046

Stcherbinine, A., Vincendon, M., Montmessin, F., Wolff, M. J., Korablev, O., Fedorova, A., et al. (2020). Martian water ice clouds during the 2018 global dust storm as observed by the ACS mid- infrared channel onboard the Trace Gas Orbiter. *Journal of Geophysical Research: Planets*, 125, e2019JE006300. https://doi.org/10.1029/2019JE006300

Streeter, P. M., Lewis, S. R., Patel, M. R., Holmes, J. A., & Kass, D. M. (2020). Surface warming during the 2018/Mars Year 34 Global Dust Storm. *Geophysical Research Letters*, 47, e2019GL083936. https://doi.org/10.1029/2019GL083936

Viúdez- Moreiras, D., Newman, C. E., de la Torre, M., Martínez, G., Guzewich, S., Lemmon, M., et al. (2019). Effects of the MY34/2018 global dust storm as measured by MSL REMS in Gale crater. *Journal of Geophysical Research: Planets*, 124, 1899– 1912. https://doi.org/10.1029/2019JE005985

Wang, H., M.I. Richardson, R.J. Wilson, A.P. Ingersoll, A.D. Toigo, and R.W. Zurek (2003), Cyclones, tides, and the origin of a cross-equatorial dust storm on Mars, Geophysical Research Letters, 30 (9), doi:10.1029/2005JE002423.

Wang, H., and Richardson, M. I. (2015). The origin, evolution, and trajectory of large dust storms on Mars during Mars Years 24-30 (1999-2011), Icarus, 251, 112-127, doi: 10.1016/j.icarus.2013.10.033.

Wilson, R. J., and K. Hamilton (1996), Comprehensive model simulation of thermal tides in the Martian atmosphere, *Journal of Atmospheric Science*, 53, 1290–1326.

Wolkenberg, P., M. Giuranna, D. Grassi, A. Aronica, S. Aoki, D. Scaccabarozzi, and B. Saggin (2018). Characterization of dust activity on Mars from MY27 to MY32 by PFS-MEX observations. Icarus, 310, 32-47, https://doi.org/10.1016/j.icarus.2017.10.045

Wolkenberg, P., Giuranna, M., Smith, M. D., Grassi, D., & Amoroso, M. (2020). Similarities and differences of global dust storms in MY 25, 28, and 34. *Journal of Geophysical Research: Planets*, 125, e2019JE006104. https://doi.org/10.1029/2019JE006104